Chapter 4
Multi-Parameter Integrated Optical Sensor Based on Multimode Interference and Microring Resonator Structures

Trung-Thanh Le

4.1. Introduction

Current approaches to the real time analysis of chemical and biological sensing applications utilize systematic approaches such as mass spectrometry for detection. Such systems are expensive, heavy and cannot monolithically integrated in one single chip [1]. Electronic sensors use metallic probes which produces electro-magnetic noise, which can disturb the electro-magnetic field being measured. This can be avoided in the case of using integrated optical sensors. Integrated optical sensors are very attractive due to their advantages of high sensitivity and ultra-wide bandwidth, low detection limit, compactness and immunity to electromagnetic interference [2, 3].

Optical sensors have been used widely in many applications such as biomedical research, healthcare and environmental monitoring. Typically, detection can be made by the optical absorption of the analytes, optic spectroscopy or the refractive index change [1]. The two former methods can be directly obtained by measuring optical intensity. The third method is to monitor various chemical and biological systems via sensing of the change in refractive index [4].

Optical waveguide devices can perform as refractive index sensors particularly when the analyte becomes a physical part of the device, such as waveguide cladding. In this case, the evanescent portion of the guided mode within the cladding will overlap and interact with the analyte. The measurement of the refractive index change of the guided mode of the optical waveguides requires a special structure to convert the refractive index change into detectable signals. A number of refractive index sensors based on optical waveguide structures have been reported, including Bragg grating sensors, directional coupler

Trung-Thanh Le
International School (VNU-IS), Vietnam National University (VNU), Cau Giay, Hanoi, Vietnam

sensors, Mach- Zehnder interferometer (MZI) sensors, microring resonator sensors and surface plasmon resonance sensors [1, 4-7].

Recently, the use of optical microring resonators as sensors [2, 6] is becoming one of the most attractive candidates for optical sensing applications because of its ultra-compact size and easy to realize an array of sensors with a large scale integration [8-10]. When detecting target chemicals by using microring resonator sensors, one can use a certain chemical binding on the surface. There are two ways to measure the presence of the target chemicals. One is to measure the shift of the resonant wavelength and the other is to measure the optical intensity with a fixed wavelength.

In the literature, some highly sensitive resonator sensors based on polymer and silicon microring and disk resonators have been developed [11-14]. However, multichannel sensors based on silicon waveguides and MMI structures, which have ultra-small bends due to the high refractive index contrast and are compatible with the existing CMOS fabrication technologies, are not presented much. In order to achieve multichannel capability, multiplexed single microring resonators must be used. This leads to large footprint area and low sensitivity. For example, recent results on using single microring resonators for glucose and ethanol detection showed that sensitivity of 108 nm/RIU [2, 15], 200 nm/RIU [16] or using microfluidics with grating for ethanol sensor with a sensitivity of 50 nm/RIU [17]. Silicon waveguide based sensors has attracted much attention for realizing ultra-compact and cheap optical sensors. In addition, the reported sensors can be capable of determining only one chemical or biological element.

The sensing structures based on one microring resonator or Mach Zender interferometer can only provide a small sensitivity and single anylate detection [13]. Therefore, in this study, we present new structures for achieving a highly sensitive and multichannel sensor. Our structures are based on only 4×4, 6×6 and 8×8 multimode interference (MMI) coupler assisted microring resonators for two, three and four parameter sensors. The proposed sensors provide very high sensitivity compared with the conventional MZI sensor. In addition, it can measure multi-parameter target chemicals and biological elements simultaneously.

4.2. Multimode Interference Structures

The conventional MMI coupler has a structure consisting of a homogeneous planar multimode waveguide region connected to a number of single mode access waveguides. The MMI region is sufficiently wide to support a large number of lateral modes. There are three main interference mechanisms. These mechanisms depend upon the locations of the access waveguides [18]. The first is the general interference (GI) mechanism which is independent of the modal excitation. The second is the restricted interference (RI) mechanism, in which excitation inputs are placed at some special positions so that certain modes are not excited. The last mechanism is the symmetric interference (SI), in which the excitation input is located at the centre of the multimode section.

The characteristics of an MMI device can be described by a transfer matrix [19-21]. This transfer matrix is a very useful tool for analyzing cascaded MMI structures. The phase ϕ_{ij} associated with imaging an input i to an output j in an MMI coupler. These phases ϕ_{ij} form a matrix $\mathbf{\Phi}$, with i representing the row number, and j representing the column number. Then the transfer matrix of the MMI coupler $\mathbf{M}$ is directly related to $\mathbf{\Phi}$, and the output field distribution emerging from the MMI coupler can be written as

$$\mathbf{b} = \mathbf{M}\mathbf{a}, \tag{4.1}$$

where $\mathbf{a} = [a_1\ a_2\ \ldots\ a_N]^T$, $\mathbf{b} = [b_1\ b_2\ \ldots\ b_N]^T$ and $\mathbf{M} = [m_{ij}]_{NxN}$. The superscript T indicates the transpose of a matrix. a_i (I = 1,..,N) is the complex field amplitude at input waveguide i and b_j (j = 1,..,N) is the complex field amplitude at output waveguide j. Elements of the transfer matrix $\mathbf{M}$ are $m_{ij} = m_{ji} = A_{ij}e^{j\phi_{ij}}$, where A_{ij} is the field amplitude transfer coefficient and ϕ_{ij} is the phase shift when imaging from input i to output j.

4.3. Microring Resonator

Consider a curved waveguide having a radius R connected to an MMI coupler to form a single microresonator as shown in Fig. 4.1.

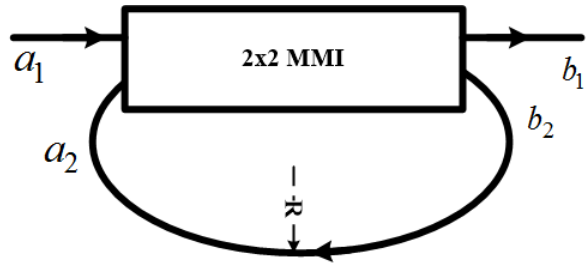

Fig. 4.1. The structure of a microresonator using a 2×2 MMI coupler.

If the common phase factor ϕ_0 of the MMI coupler is factored out for simplicity, then the complex amplitudes of the input signals a_i (i=1, 2) and output signals b_j (j=1, 2) are related through the transfer matrix of the 2×2 MMI coupler [22]

$$\mathbf{b} = \mathbf{M}\mathbf{a}, \tag{4.2}$$

$$\text{where } \mathbf{M} = \begin{pmatrix} \tau & \kappa \\ -\kappa^* & \tau^* \end{pmatrix}, \ \mathbf{a} = [a_1 \ a_2]^T \text{ and } \mathbf{b} = [b_1 \ b_2]^T. \tag{4.3}$$

Here τ and κ are the amplitude transmission and coupling coefficients of the coupler, respectively. The superscripts * and T denote the complex conjugate and the transpose of a matrix, respectively. For a lossless coupler, $|\kappa|^2 + |\tau|^2 = 1$. A plot of the transmission characteristics as a function of microresonator loss factor (α), with transmission coefficient $|\tau|$ as parameter, is presented in Fig. 4.2. The transmission loss factor α is $\alpha = \exp(-\alpha_0 L_R)$, where L_R is the total length of the racetrack (or ring) waveguide and $\alpha_0 (\text{dB/cm})$ is the transmission loss coefficient.

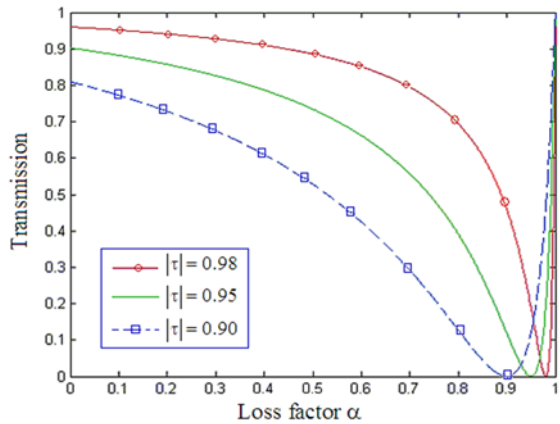

Fig. 4.2. The transmission characteristic of a single microresonator based on a 2×2 MMI.

By rapidly changing the loss/gain or the coupling coefficient of the coupler, optical modulators and optical switches can be created. In addition, a single microresonator can be used as an optical notch filter. The spectral response of the microresonator is shown in Fig. 4.3, for a loss factor of α = 0.7. Here, θ is the phase accumulated inside the microresonator, $\theta = -\beta_0 (2\pi R + L')$, where β_0 is the propagation constant, L' is the length shown in Fig. 4.3 and R is the radius of the curved waveguide. The simulations show that the largest extinction ratio can be achieved with critical coupling that is when the loss factor α equals the transmission coefficient $|\tau|$ ($\alpha = |\tau|$).

4.4. Two-Parameter Sensor Based on 4×4 MMI and Resonator Structure

We present a structure for achieving a highly sensitive and multichannel sensor. Our structure is based on only one 4×4 multimode interference (MMI) coupler assisted microring resonators [23, 24]. The proposed sensors provide very high sensitivity compared with the conventional MZI sensors. In addition, it can measure two different

and independent target chemicals and biological elements simultaneously. We investigate the use of our proposed structure to glucose and ethanol sensing at the same time. The proposed sensor based on 4×4 multimode interference and microring resonator structures is shown in Fig. 4.4. The two MMI couplers are identical. The two 4×4 MMI couplers have the same width W_{MMI} and length L_{MMI}.

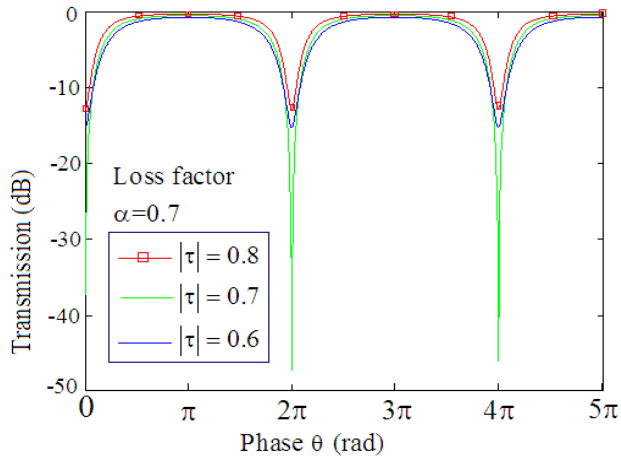

Fig. 4.3. Transmission characteristic of a single microresonator.

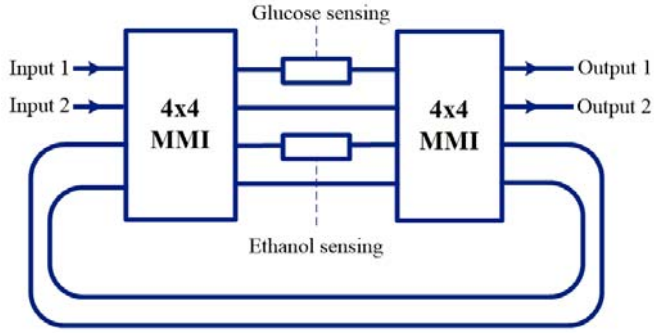

Fig. 4.4. Schematic of the new sensor using 4×4 MMI couplers and microring resonators.

In this structure, there are two sensing windows having lengths L_{arm1}, L_{arm2}. As with the conventional MZI sensor device, segments of two MZI arms overlap with the flow channel, forming two separate sensing regions. The other two MZI arms isolated from the analyte by the micro fluidic substrate. The MMI coupler consists of a multimode optical waveguide that can support a number of modes [25]. In order to launch and extract light from the multimode region, a number of single mode access waveguides are placed at the input and output planes. If there are N input waveguides and M output waveguides, then the device is called an NxM MMI coupler.

In this study, the access waveguides are identical single mode waveguides with width W_a. The input and output waveguides are located at [18]

$$x_i = (i + \frac{1}{2})\frac{W_{MMI}}{N}, \ (i = 0, 1, \ldots, N\text{-}1). \tag{4.4}$$

The electrical field inside the MMI coupler can be expressed by [19]

$$E(x,z) = \exp(-jkz)\sum_{m=1}^{M} E_m \exp(j\frac{m^2\pi}{4\Lambda}z)\sin(\frac{m\pi}{W_{MMI}}x). \tag{4.5}$$

If we choose the MMI coupler having a length of $L_{MMI} = \frac{3L_\pi}{2}$, where L_π is the beat length of the MMI coupler [26]. One can prove that the normalized optical powers transmitted through the proposed sensor at wavelengths on resonance with the microring resonators are given by [9]

$$T_1 = \left\{\frac{\alpha_1 - \left|\cos(\frac{\Delta\varphi_1}{2})\right|}{1 - \alpha_1\left|\cos(\frac{\Delta\varphi_1}{2})\right|}\right\}^2, \tag{4.6}$$

$$T_2 = \left\{\frac{\alpha_2 - \left|\cos(\frac{\Delta\varphi_2}{2})\right|}{1 - \alpha_2\left|\cos(\frac{\Delta\varphi_2}{2})\right|}\right\}^2, \tag{4.7}$$

where $\tau_1 = \sin(\frac{\Delta\varphi_1}{2})$, $\kappa_1 = \cos(\frac{\Delta\varphi_1}{2})$ $\tau_2 = \sin(\frac{\Delta\varphi_2}{2})$, and $\kappa_2 = \cos(\frac{\Delta\varphi_2}{2})$; $\Delta\varphi_1$, $\Delta\varphi_2$ are the phase differences between two arms of the MZI, respectively; α_1, α_2 are round trip transmissions of light propagation through the two microring resonators [27].

In this study, the locations of input, output waveguides, MMI width and length are carefully designed, so the desired characteristics of the MMI coupler can be achieved. It is now shown that the proposed sensor can be realized using silicon nanowire waveguides [28, 29]. By using the numerical method, the optimal width of the MMI is calculated to be $W_{MMI} = 6\mu m$ for high performance and compact device. The core thickness is h_{co} = 220 nm. The access waveguide is tapered from a width of 500 nm to a width of 800 nm to improve device performance. It is assumed that the designs are for the transverse electric (TE) polarization at a central optical wavelength $\lambda = 1550\ nm$. The FDTD simulations for sensing operation when input signal is at port 1 and port 2 for

glucose and ethanol sensing are shown in Fig. 4.5 (a) and 4.5 (b), respectively. The mask design for the whole sensor structure using CMOS technology is shown in Fig. 4.5 (c).

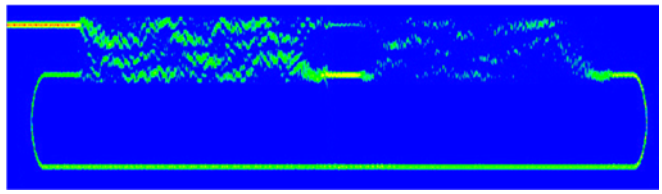

(a) Input 1, glucose sensing

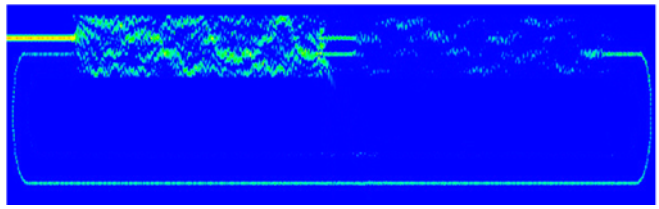

(b) Input 2, Ethanol sensing

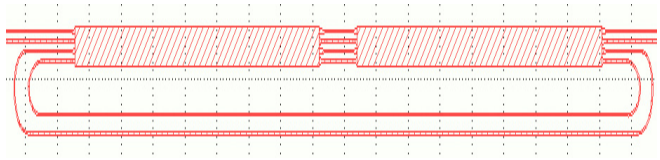

(c) Mask design

Fig. 4.5. FDTD simulations for two-channel sensors (a) glucose; (b) Ethanol and (c) mask design.

The proposed structure can be viewed as a sensor with two channel sensing windows, which are separated with two power transmission characteristics T_1, T_2 and sensitivities S_1, S_2. When the analyte is presented, the resonance wavelengths are shifted. As the result, the proposed sensors are able to monitor two target chemicals simultaneously and their sensitivities can be expressed by:

$$S_1 = \frac{\partial \lambda_1}{\partial n_c}, \; S_2 = \frac{\partial \lambda_2}{\partial n_c}, \tag{4.8}$$

where λ_1 and λ_2 are resonance wavelengths of the transmissions at output 1 and 2, respectively.

For the conventional sensor based on MZI structure, the relative phase shift $\Delta\varphi$ between two MZI arms and the optical power transmitted through the MZI can be made a function of the environmental refractive index, via the modal effective index n_{eff}. The transmission at the bar port of the MZI structure can be given by [1]

$$T_{MZI} = \cos^2(\frac{\Delta\varphi}{2}), \tag{4.9}$$

where $\Delta\varphi = 2\pi L_{arm}(n_{eff,a} - n_{eff,0})/\lambda$, L_{arm} is the interaction length of the MZI arm, $n_{eff,a}$ is effective refractive index in the interaction arm when the ambient analyte is presented and $n_{eff,0}$ is effective refractive index of the reference arm.

The sensitivity S_{MZI} of the MZI sensor is defined as a change in normalized transmission per unit change in the refractive index and can be expressed as

$$S_{MZI} = \frac{\partial T_{MZI}}{\partial n_c}, \tag{4.10}$$

where n_c is the cover medium refractive index or the refractive index of the analyte. The sensitivity of the MZI sensor can be rewritten by

$$S_{MZI} = \frac{\partial T_{MZI}}{\partial n_c} = \frac{\partial T_{MZI}}{\partial n_{eff,a}} \frac{\partial n_{eff,a}}{\partial n_c}. \tag{4.11}$$

The waveguide sensitivity parameter $\frac{\partial n_{eff,a}}{\partial n_c}$ can be calculated using the variation theorem for optical waveguides [1]:

$$\frac{\partial n_{eff,a}}{\partial n_c} = \frac{\frac{n_c}{n_{eff,a}} \iint\limits_{analyte} |E_a(x,y)|^2 \, dxdy}{\iint\limits_{\infty} |E_a(x,y)|^2 \, dxdy}, \tag{4.12}$$

where $E_a(x,y)$ is the transverse field profile of the optical mode within the sensing region, calculated assuming a dielectric material with index n_c occupies the appropriate part of the cross-section. The integral in the numerator is carried out over the fraction of the waveguide cross-section occupied by the analyte and the integral in the denominator is carried out over the whole cross-section.

For sensing applications, sensor should have steeper slopes on the transmission and phase shift curve for higher sensitivity. From (4.9) and (4.10), we see that the sensitivity of the MZI sensor is maximized at phase shift $\Delta\varphi = 0.5\pi$. Therefore, the sensitivity of the MZI sensor can be enhanced by increasing the sensing window length L_a or increasing the waveguide sensitivity factor $\frac{\partial n_{eff,a}}{\partial n_c}$, which can be obtained by properly designing optical waveguide structure. In this chapter, we present a new sensor structure based on microring resonators for very high sensitive and multi-channel sensing applications.

From equations (4.8) and (4.10), the ratio of the sensitivities of the proposed sensor and the conventional MZI sensor can be numerically evaluated. The sensitivity enhancement factor S_1 / S_{MZI} can be calculated for values of α_1 between 0 and 1 is plotted in Fig. 4.6. For $\alpha_1 = 0.99$, an enhancement factor of approximately 10 is obtained. The similar results can be achieved for other sensing arms.

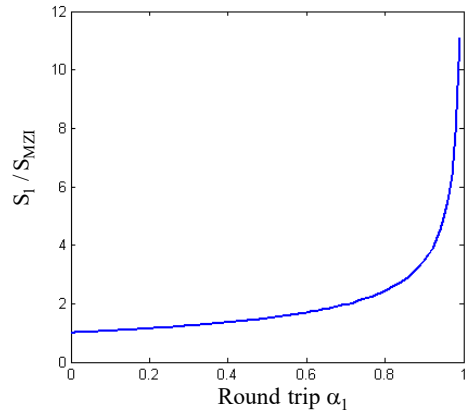

Fig. 4.6. Sensitivity enhancement factor for the proposed sensor, calculated with the first sensing arm.

In general, our proposed structure can be used for detection of chemical and biological elements by using both surface and homogeneous mechanisms. Without loss of generality, we applied our structure to detection of glucose and ethanol sensing as an example. The refractive indexes of the glucose ($n_{glucose}$) and ethanol (n_{EtOH}) can be calculated from the concentration (C %) based on experimental results at wavelength 1550 nm by [30-32]

$$n_{glucose} = 0.2015 \times [C] + 1.3292, \tag{4.13}$$

$$n_{EtOH} = 1.3292 + a[C] + b[C]^2, \tag{4.14}$$

where $a = (8.4535 \times 10^{-4})$ and $b = -(4.8294 \times 10^{-6})$. The refractive indexes of the glucose and EtOH at different concentrations are shown in Fig. 4.7. In our design, the silicon waveguide with a height of 220 nm, width of 500 nm is used for single mode operation. The wavelength is at 1550 nm. It is assumed that the interaction lengths for glucose and ethanol sensing arms are $100\,\mu m$. By using the finite difference method (FDM), the effective refractive indexes of the waveguide at different concentration is shown in Fig. 4.8.

The glucose solutions with concentrations of 0 %, 0.2 % and 0.4 % and Ethanol concentrations of 0 %, 3 % and 6 % are induced to the device. The resonance wavelength shifts corresponding to the concentrations can be measured by the optical spectrometer as

shown in Fig. 4.9 for glucose and Fig. 4.10 for ethanol. For each 0.2 % increment of the glucose concentration, the resonance wavelength shifts of about 10^5 pm is achieved. This is a greatly higher order than that of the recent conventional sensor based on single microring resonator [31, 33]. For each 3 % increment of the ethanol concentration, the resonance wavelength shifts of about 1.5×10^4 pm is achieved.

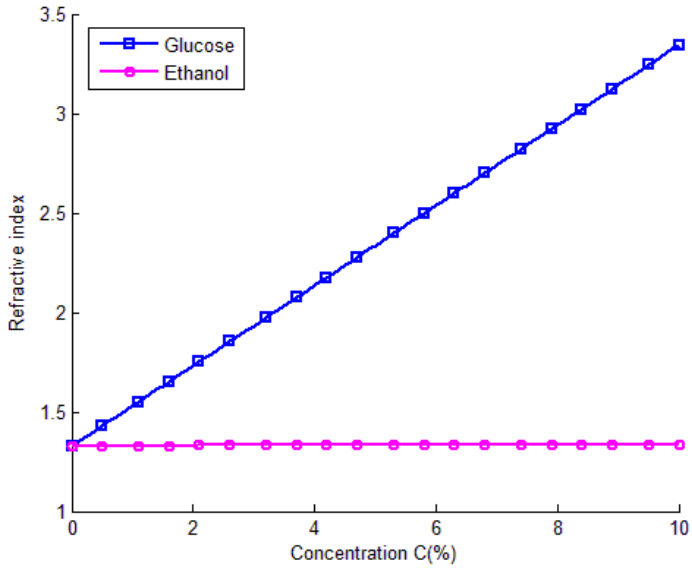

Fig. 4.7. Refractive indexes of the glucose and ethanol vs. concentations.

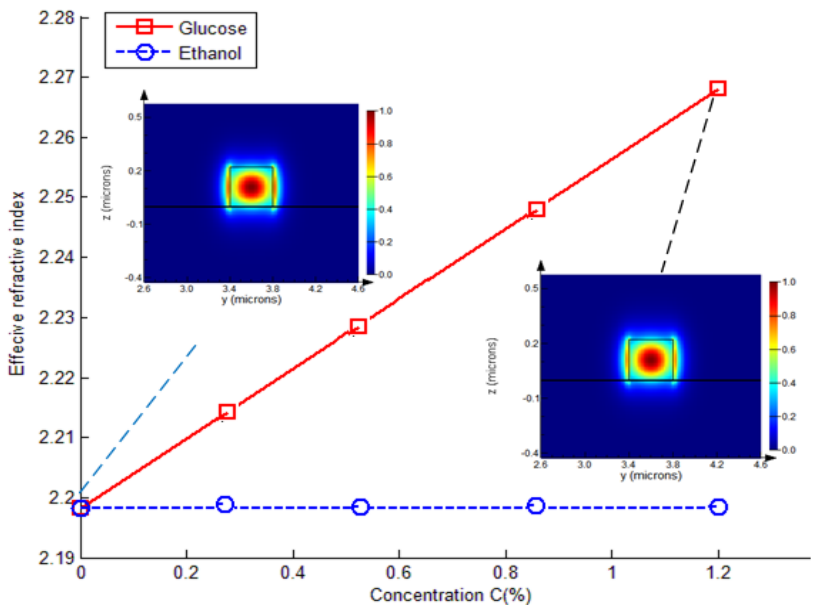

Fig. 4.8. Effective refractive indexes of the waveguide with glucose and ethanol cover at different concentrations.

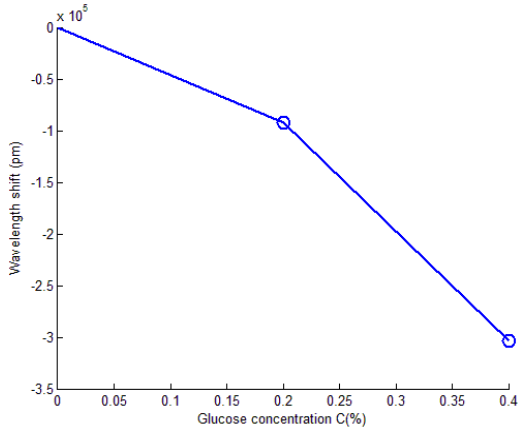

Fig. 4.9. Resonance wavelength shift at different glucose concentrations.

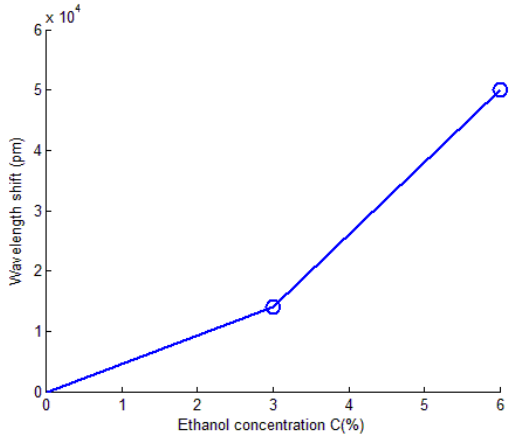

Fig. 4.10. Resonance wavelength shift at different ethanol concentrations.

By measuring the resonance wavelength shift ($\Delta\lambda$), the glucose concentration is detected. The sensitivity of the glucose sensor can be calculated by

$$S_{glucose} = \frac{\Delta\lambda}{\Delta n} = 9000(\text{nm/ RIU}). \tag{4.15}$$

Our sensor provides the sensitivity of 9000 nm/RIU compared with a sensitivity of 170 nm/RIU [33].

In addition to the sensitivity, the detection limit (DL) is another important parameter. For the refractive index sensing, the DL presents for the smallest ambient refractive index change, which can be accurately measured. The Detection limit (DL) can be calculated as the ratio of the resonance wavelength resolution σ to the sensitivity $S_{glucose}$ by [34]

$$DL = \frac{\sigma}{S_{glucose}}, \tag{4.16}$$

where $\sigma = \sqrt{\sigma_{amp-noise}^2 + \sigma_{temp-induced}^2 + \sigma_{spec-res}^2}$, $\sigma_{amp-noise}$ is the standard deviation of the spectral variation which is determined by the Q factor and extinction ratio, $\sigma_{temp-induced}$ is the standard deviation induced by noises in the sensing systems and $\sigma_{spec-res}$ is resulted from the spectral resolution of the optical spectrometer. In our sensor design, we use the optical refractometer with a resolution of 20 pm, the detection limit of our sensor is calculated to be 2×10^{-4}, compared with a detection limit of 1.78×10^{-5} of single microring resonator sensor [35]. The sensitivity of the ethanol sensor is calculated to be $S_{EtOH} = 6000\,(\text{nm/ RIU})$ and detection limit is 1.3×10^{-5}.

It is noted that silicon waveguides are highly sensitive to temperature fluctuations due to the high thermo-optic coefficient (TOC) of silicon ($TOC_{Si} = 1.86\times10^{-4}K^{-1}$). As a result, the sensing performance will be affected due to the phase drift. In order to overcome the effect of the temperature and phase fluctuations, we can use some approaches including of both active and passive methods. For example, the local heating of silicon itself to dynamically compensate for any temperature fluctuations [36], material cladding with negative thermo-optic coefficient [37-40], MZI cascading intensity interrogation [14], control of the thermal drift by tailoring the degree of optical confinement in silicon waveguides with different waveguide widths [41], ultra-thin silicon waveguides [42] can be used for reducing the thermal drift.

4.5. Three-Parameter Sensor Based on 6×6 MMI and Resonator Structure

The proposed sensor based on 6×6 multimode interference and microring resonator structures is shown in Fig. 4.11 [9]. The two MMI couplers are identical. The two 6×6 MMI couplers have the same width W_{MMI} and length L_{MMI}. In this structure, there are three sensing windows having lengths L_{a1}, L_{a2}, L_{a3}. As with the conventional MZI sensor device, segments of four MZI arms having lengths L_{a1}, L_{a2}, L_{a3} overlap with the flow channel, forming three separate sensing regions. The other three MZI arms isolated from the analyte by the micro fluidic circuit's substrate.

If we choose the MMI coupler having a length of $L_{MMI} = \frac{3L_\pi}{2}$, where L_π is the beat length of the MMI coupler, $L_\pi = \frac{\pi}{\beta_1 - \beta_2}$; the MMI coupler is characterized by a transfer matrix M. We can prove that the overall transfer matrix S of both the MMI coupler and combiner in Fig. 4.11 is expressed by

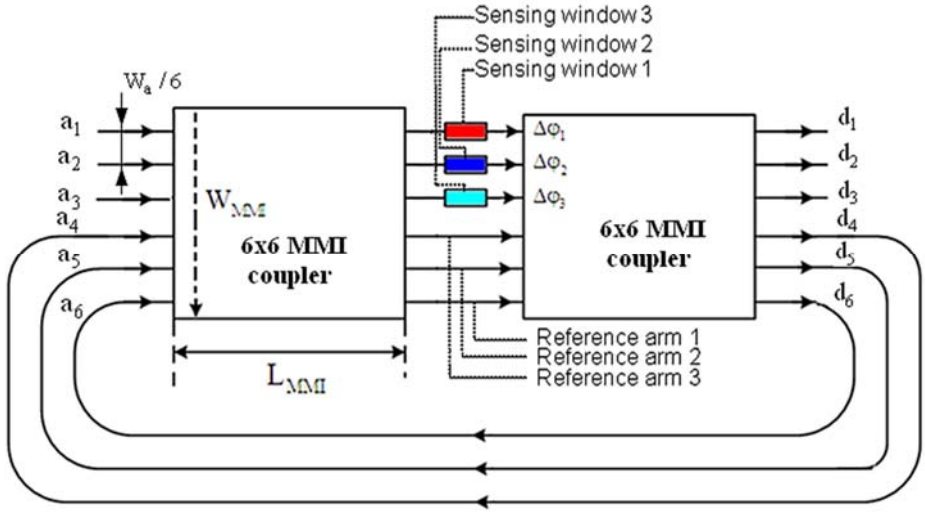

Fig. 4.11. Schematic of the new sensor using 6×6 MMI couplers and microring resonators. Four arms of the MZI is exposed to the analyte within the interaction regions

$$\mathbf{S} = \frac{1}{\sqrt{2}} \begin{bmatrix} e^{j\frac{\pi}{4}} & 0 & 0 & 0 & 0 & e^{j\frac{3\pi}{4}} \\ 0 & e^{j\frac{\pi}{4}} & 0 & 0 & e^{j\frac{3\pi}{4}} & 0 \\ 0 & 0 & e^{j\frac{\pi}{4}} & e^{j\frac{3\pi}{4}} & 0 & 0 \\ 0 & 0 & e^{j\frac{3\pi}{4}} & e^{j\frac{\pi}{4}} & 0 & 0 \\ 0 & e^{j\frac{3\pi}{4}} & 0 & 0 & e^{j\frac{\pi}{4}} & 0 \\ e^{j\frac{3\pi}{4}} & 0 & 0 & 0 & 0 & e^{j\frac{\pi}{4}} \end{bmatrix}. \tag{4.17}$$

This matrix can be considered as consisting of four separate sub-matrices which describe four 2×2 3 dB MMI couplers, both having the transfer matrix

$$\mathbf{M_2} = \frac{1}{\sqrt{2}} \begin{bmatrix} e^{j\frac{\pi}{4}} & e^{j\frac{3\pi}{4}} \\ e^{j\frac{3\pi}{4}} & e^{j\frac{\pi}{4}} \end{bmatrix} = \frac{1}{\sqrt{2}} e^{j\frac{\pi}{4}} \begin{bmatrix} 1 & j \\ j & 1 \end{bmatrix}. \tag{4.18}$$

Relations between the complex amplitudes $a_1, a_2, ..., a_6$ at the input ports and $d_1, d_2, ..., d_6$ at the output ports can be expressed in terms of the transfer matrices of the 3 dB MMI couplers and the phase shifters as follows

$$\begin{bmatrix} d_1 \\ d_6 \end{bmatrix} = je^{j\frac{\Delta\varphi_1}{2}} \begin{bmatrix} \tau_1 & \kappa_1 \\ \kappa_1^* & -\tau_1^* \end{bmatrix} \begin{bmatrix} a_1 \\ a_6 \end{bmatrix}, \tag{4.19}$$

$$\begin{bmatrix} d_2 \\ d_5 \end{bmatrix} = je^{j\frac{\Delta\varphi_2}{2}} \begin{bmatrix} \tau_2 & \kappa_2 \\ \kappa_2^* & -\tau_2^* \end{bmatrix} \begin{bmatrix} a_2 \\ a_5 \end{bmatrix}, \tag{4.20}$$

$$\begin{bmatrix} d_3 \\ d_4 \end{bmatrix} = je^{j\frac{\Delta\varphi_1}{2}} \begin{bmatrix} \tau_3 & \kappa_3 \\ \kappa_3^* & -\tau_3^* \end{bmatrix} \begin{bmatrix} a_3 \\ a_4 \end{bmatrix}, \tag{4.21}$$

where $\tau_1 = \sin(\frac{\Delta\varphi_1}{2}), \kappa_1 = \cos(\frac{\Delta\varphi_1}{2})$; $\tau_2 = \sin(\frac{\Delta\varphi_2}{2}), \kappa_2 = \cos(\frac{\Delta\varphi_2}{2})$; $\tau_3 = \sin(\frac{\Delta\varphi_3}{2}), \kappa_3 = \cos(\frac{\Delta\varphi_3}{2})$; $\Delta\varphi_1$, $\Delta\varphi_2$, $\Delta\varphi_3$ are the phase differences between two arms of the MZI, respectively.

One can prove that the normalized optical powers transmitted through the proposed sensor at wavelengths on resonance with the microring resonators are given by

$$T_1 = \left|\frac{d_1}{a_1}\right|^2 = \left[\frac{\alpha_1 - \left|\cos(\frac{\Delta\varphi_1}{2})\right|}{1 - \alpha_1\left|\cos(\frac{\Delta\varphi_1}{2})\right|}\right]^2, \tag{4.22}$$

$$T_2 = \left|\frac{d_2}{a_2}\right|^2 = \left[\frac{\alpha_2 - \left|\cos(\frac{\Delta\varphi_2}{2})\right|}{1 - \alpha_2\left|\cos(\frac{\Delta\varphi_2}{2})\right|}\right]^2, \tag{4.23}$$

$$T_3 = \left|\frac{d_3}{a_3}\right|^2 = \left[\frac{\alpha_3 - \left|\cos(\frac{\Delta\varphi_3}{2})\right|}{1 - \alpha_3\left|\cos(\frac{\Delta\varphi_3}{2})\right|}\right]^2, \tag{4.24}$$

where α_1, α_2, and α_3 are round trip transmissions of light propagation through the four microring resonators [27] depending the losses of light propagation from output ports d_4, d_5, d_6 back to input ports a_4, a_5, a_5; for a lossless resonator $\alpha = 1$. The proposed structure can be viewed as a sensor with four channel sensing windows, which are separated with four power transmission characteristics T_1, T_2, and T_3 and four sensitivities S_1, S_2 and S_3. This means that the proposed sensor is able to monitor four target chemicals simultaneously. Their sensitivities can be expressed by:

$$S_1 = \frac{\partial T_1}{\partial n_c}, S_2 = \frac{\partial T_2}{\partial n_c}, S_3 = \frac{\partial T_3}{\partial n_c}. \quad (4.25)$$

Fig. 4.12 compares the normalized transmission for the proposed sensor with $\alpha_1 = 0.99$ and 0.90 to that for the conventional MZI, as functions of the total relative phase $\Delta\varphi$. Given that the sensitivity is linearly proportional to the slope of the power transfer characteristics. Fig. 4.12 shows that the proposed sensor should have a higher sensitivity to a change in the refractive index of the analyte than the conventional MZI, when biased for operation with the region of large slope near $\Delta\varphi_1 = 0$.

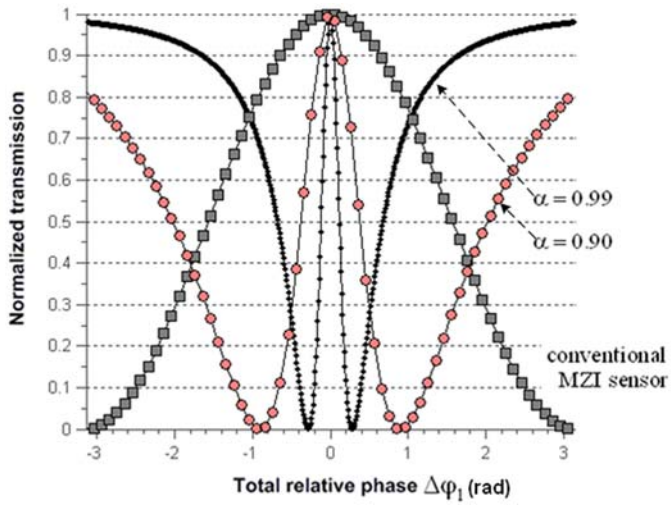

Fig. 4.12. Normalized optical transmissions as functions of total relative phase for the proposed sensor with $\alpha_1 = 0.99$ and 0.90 and conventional MZI sensor.

It is now shown that the proposed sensor can be realized using silicon nanowire waveguides. The width of the MMI is $W_{MMI} = 8.4\,\mu m$ and the core thickness is h_{co} = 220 nm. The access waveguide is tapered to a width of 0.8 μm to improve device performance. It is assumed that the designs are for the transverse electric (TE) polarization at a central optical wavelength $\lambda = 1550\,nm$.

The first 6×6 MMI coupler is now optimized by using the 3D BPM. Fig. 4.13 (a) shows the normalized output powers at the bar and cross ports at different MMI lengths for a signal presented at input port 1 of the MMI coupler. From this simulation result, the optimized length of MMI calculated to be $L_{MMI} = 273.5\,\mu m$. The field propagation through the 6×6 MMI coupler at this optimized length is plotted in Fig. 4.13 (b).

The relation between the effective index $n_{eff,a}$ and the ambient index or cladding index $n_{analyte} = n_c$ is achieved by using the beam propagation method (BPM). From this

relationship, we achieve the waveguide sensitivity factor $\frac{\partial n_{eff,a}}{\partial n_c}$. Fig. 4.14 shows the effective index change $\delta n_{eff,a}$ due to the ambient change for silicon nanowire waveguides having a width of 500 nm. We can see that effective index $n_{eff,a}$ increases almost linearly in the change in the refractive index of ambient material, i.e., the waveguide sensitivity factor is almost a constant.

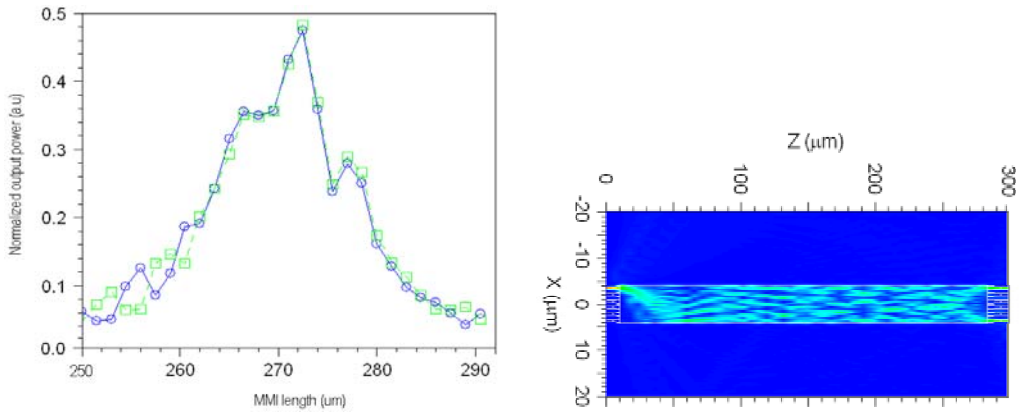

(a) Normalized output powers vs MMI length. (b) Field propagation.

Fig. 4.13. BPM simulation results: (a) Normalized output powers vs the length of the 6×6 MMI coupler, and (b) field propagation at the optimized MMI length.

From the simulation results of Fig. 4.14, the sensitivities of the proposed sensor and the conventional MZI with the active region length of $L_a = 100\,\mu m$ and $L_a = 500\,\mu m$ are plotted in Fig. 4.15. The simulations obviously show that the sensitivity of the proposed sensor is much higher than the sensitivity of the conventional MZI sensor.

4.6. Four-Parameter Sensor Based on 8×8 MMI and Resonator Structure

The proposed sensor based on 8×8 multimode interference and microring resonator structures is shown in Fig. 4.16 [43]. The two 8×8 MMI couplers have the same width W_{MMI} and length L_{MMI}. There are four sensing windows having lengths $L_{a1}, L_{a2}, L_{a3}, L_{a4}$. As with the conventional MZI sensor device, segments of four MZI arms having lengths $L_{a1}, L_{a2}, L_{a3}, L_{a4}$ overlap with the flow channel, forming four separate sensing regions. As a result, this structure can be used to detect four chemical or analyates at the same time.

If we choose the MMI coupler having a length of $L_2 = 3L_\pi / 4$, the overall transfer matrix S of both the MMI coupler and combiner of length $L_{MMI} = 3L_\pi / 2$ is expressed by [43]

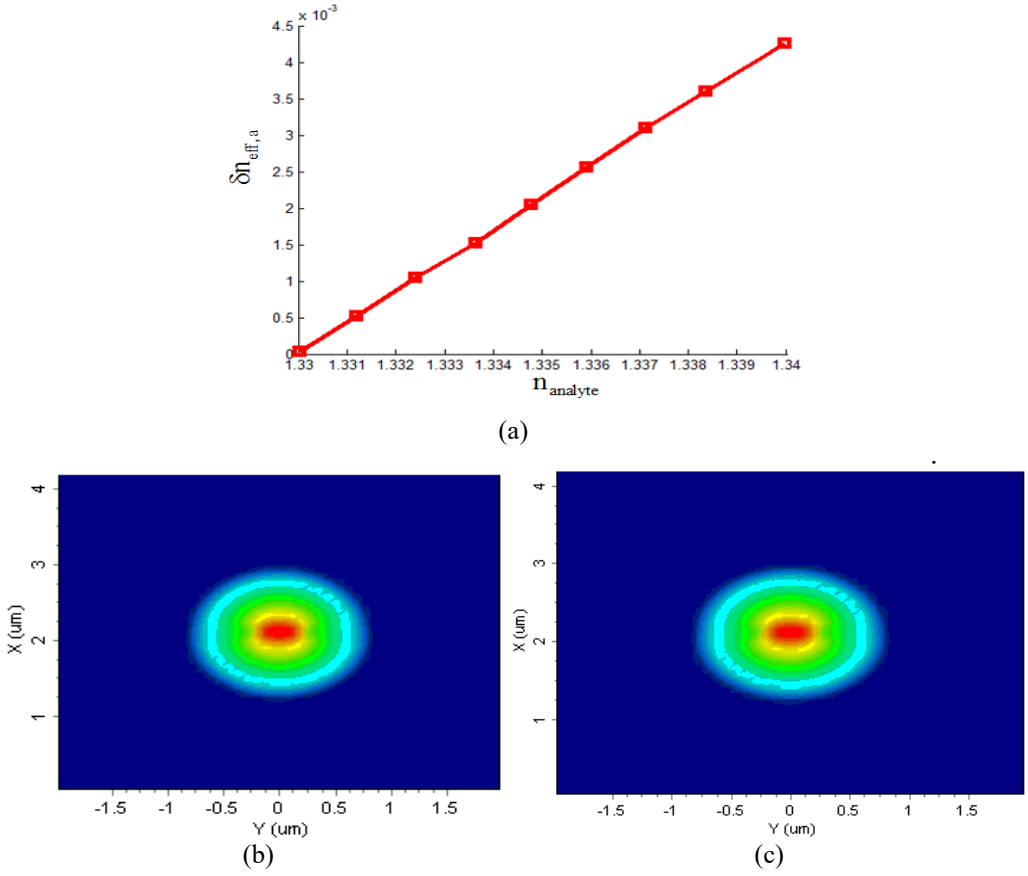

Fig. 4.14. (a) The change of the effective index as the increase of refractive index of the analyte for silicon nanowire waveguides; (b) optical field profile for $n_{analyte} = 1.33$ and (c) optical field profile for $n_{analyte} = 1.34$.

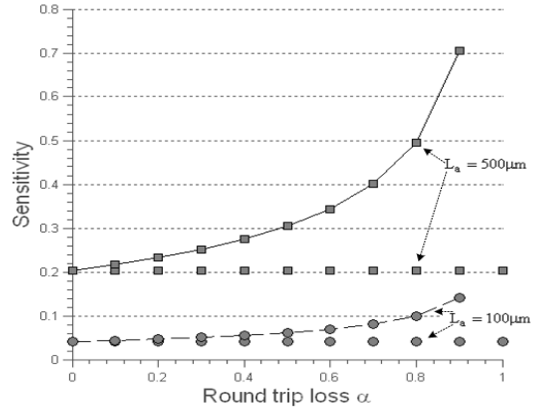

Fig. 4.15. Sensitivity of the proposed sensor for sensing window S1 and the conventional MZI sensor versus the round trip loss of the first microring resonator.

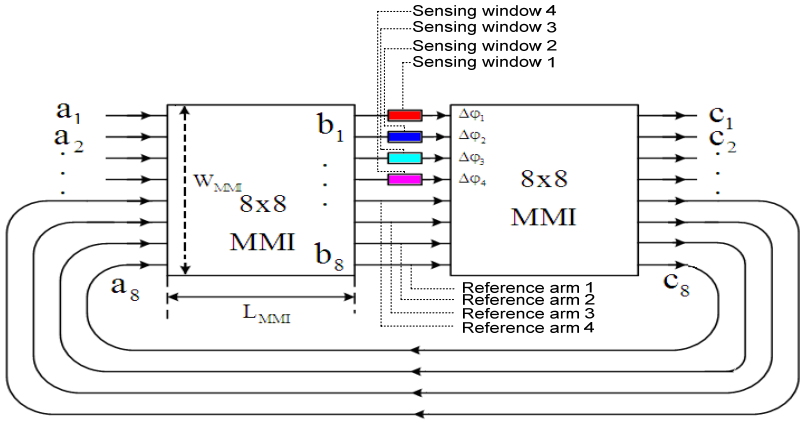

Fig. 4.16. Schematic of the new sensor using 8×8 MMI couplers and microring resonators.

$$\mathbf{S} = \frac{1}{\sqrt{2}} \begin{bmatrix} e^{j\frac{\pi}{4}} & 0 & 0 & 0 & 0 & 0 & 0 & e^{j\frac{3\pi}{4}} \\ 0 & e^{j\frac{\pi}{4}} & 0 & 0 & 0 & 0 & e^{j\frac{3\pi}{4}} & 0 \\ 0 & 0 & e^{j\frac{\pi}{4}} & 0 & 0 & e^{j\frac{\pi}{4}} & 0 & 0 \\ 0 & 0 & 0 & e^{j\frac{\pi}{4}} & e^{j\frac{3\pi}{4}} & 0 & 0 & 0 \\ 0 & 0 & 0 & e^{j\frac{3\pi}{4}} & e^{j\frac{\pi}{4}} & 0 & 0 & 0 \\ 0 & 0 & e^{j\frac{3\pi}{4}} & 0 & 0 & e^{j\frac{\pi}{4}} & 0 & 0 \\ 0 & e^{j\frac{3\pi}{4}} & 0 & 0 & 0 & 0 & e^{j\frac{\pi}{4}} & 0 \\ e^{j\frac{3\pi}{4}} & 0 & 0 & 0 & 0 & 0 & 0 & e^{j\frac{\pi}{4}} \end{bmatrix}. \tag{4.26}$$

The 3D-BPM simulations for optimised designs of 8×8 MMI structures based on an SOI channel waveguide having a width of $W_{MMI} = 9\,\mu m$ are shown in Fig. 4.17. The optimised length calculated to be $L_{MMI} \approx 382\,\mu m$.

It is note that the complete device is also equivalent to four separate 2×2 MMI-based microresonators. Each microresonator may have different transmission characteristics such as different quality factor (Q), different free spectral range (FSR) and different bandwidth.

The 3D-BPM simulations show that the device performs the functions as predicted by the theory. However, when the signal is applied to input port 1, then 3D-BPM simulations show that at the optimised length of $L_{MMI} = 382\,\mu m$, the computed excess loss is 1.08 dB and the imbalance is 0.11 dB. The normalized output powers at the bar and cross ports at different MMI lengths for a signal at input port 1 are shown in Fig. 4.18.

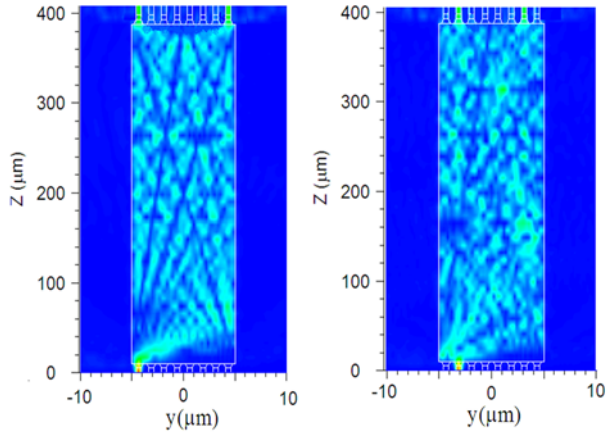

Fig. 4.17. 3D-BPM simulations of an 8×8 MMI structure used in a microresonator for two cases (a) the signal entered at input port 1, and (b) signal entered at input port 2.

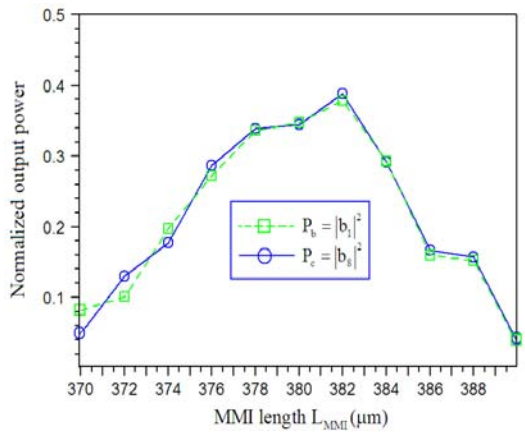

Fig. 4.18. Normalized output powers at the bar and cross ports as functions of the MMI length for the signal at input port 1.

The complex amplitudes at the output ports of the sensor structure in Fig. 4.16 can be expressed by

$$\begin{bmatrix} c_1 \\ c_8 \end{bmatrix} = \frac{1}{\sqrt{2}} e^{j\frac{\pi}{4}} \begin{bmatrix} 1 & j \\ j & 1 \end{bmatrix} \begin{bmatrix} e^{j\Delta\varphi_1} & 0 \\ 0 & 1 \end{bmatrix} \frac{1}{\sqrt{2}} e^{j\frac{\pi}{4}} \begin{bmatrix} 1 & j \\ j & 1 \end{bmatrix} \begin{bmatrix} a_1 \\ a_8 \end{bmatrix} = j e^{j\frac{\Delta\varphi_1}{2}} \begin{bmatrix} \tau_1 & \kappa_1 \\ \kappa_1^* & -\tau_1^* \end{bmatrix} \begin{bmatrix} a_1 \\ a_8 \end{bmatrix}, \tag{4.27}$$

$$\begin{bmatrix} c_2 \\ c_7 \end{bmatrix} = \frac{1}{\sqrt{2}} e^{j\frac{\pi}{4}} \begin{bmatrix} 1 & j \\ j & 1 \end{bmatrix} \begin{bmatrix} e^{j\Delta\varphi_2} & 0 \\ 0 & 1 \end{bmatrix} \frac{1}{\sqrt{2}} e^{j\frac{\pi}{4}} \begin{bmatrix} 1 & j \\ j & 1 \end{bmatrix} \begin{bmatrix} a_2 \\ a_7 \end{bmatrix} = j e^{j\frac{\Delta\varphi_2}{2}} \begin{bmatrix} \tau_2 & \kappa_2 \\ \kappa_2^* & -\tau_2^* \end{bmatrix} \begin{bmatrix} a_2 \\ a_7 \end{bmatrix}, \tag{4.28}$$

$$\begin{bmatrix} c_3 \\ c_6 \end{bmatrix} = \frac{1}{\sqrt{2}} e^{j\frac{\pi}{4}} \begin{bmatrix} 1 & j \\ j & 1 \end{bmatrix} \begin{bmatrix} e^{j\Delta\varphi_3} & 0 \\ 0 & 1 \end{bmatrix} \frac{1}{\sqrt{2}} e^{j\frac{\pi}{4}} \begin{bmatrix} 1 & j \\ j & 1 \end{bmatrix} \begin{bmatrix} a_3 \\ a_6 \end{bmatrix} = je^{j\frac{\Delta\varphi_1}{2}} \begin{bmatrix} \tau_3 & \kappa_3 \\ \kappa_3^* & -\tau_3^* \end{bmatrix} \begin{bmatrix} a_3 \\ a_6 \end{bmatrix}, \tag{4.29}$$

$$\begin{bmatrix} c_4 \\ c_5 \end{bmatrix} = \frac{1}{\sqrt{2}} e^{j\frac{\pi}{4}} \begin{bmatrix} 1 & j \\ j & 1 \end{bmatrix} \begin{bmatrix} e^{j\Delta\varphi_4} & 0 \\ 0 & 1 \end{bmatrix} \frac{1}{\sqrt{2}} e^{j\frac{\pi}{4}} \begin{bmatrix} 1 & j \\ j & 1 \end{bmatrix} \begin{bmatrix} a_4 \\ a_5 \end{bmatrix} = je^{j\frac{\Delta\varphi_2}{2}} \begin{bmatrix} \tau_4 & \kappa_4 \\ \kappa_4^* & -\tau_4^* \end{bmatrix} \begin{bmatrix} a_4 \\ a_5 \end{bmatrix}, \tag{4.30}$$

where $\mathbf{a} = [a_1\ a_2\ a_3\ a_4\ a_5\ a_6\ a_7\ a_8]^T$ is the input field and $\mathbf{c} = [c_1\ c_2\ c_3\ c_4\ c_5\ c_6\ c_7\ c_8]^T$ is the output field and $\tau_1 = \sin(\frac{\Delta\varphi_1}{2}), \kappa_1 = \cos(\frac{\Delta\varphi_1}{2}); \quad \tau_2 = \sin(\frac{\Delta\varphi_2}{2}), \kappa_2 = \cos(\frac{\Delta\varphi_2}{2});$ $\tau_3 = \sin(\frac{\Delta\varphi_3}{2}), \kappa_3 = \cos(\frac{\Delta\varphi_3}{2})$; $\tau_4 = \sin(\frac{\Delta\varphi_4}{2}), \kappa_4 = \cos(\frac{\Delta\varphi_4}{2})$. $\Delta\varphi_1$, $\Delta\varphi_2$, $\Delta\varphi_3$ and $\Delta\varphi_4$ are the phase differences between two arms of the MZI, respectively.

The normalized optical powers transmitted through the proposed sensor at wavelengths on resonance with the microring resonators are given by

$$T_1 = \left|\frac{c_1}{a_1}\right|^2 = \left[\frac{\alpha_1 - \left|\cos(\frac{\Delta\varphi_1}{2})\right|}{1 - \alpha_1\left|\cos(\frac{\Delta\varphi_1}{2})\right|}\right]^2, \tag{4.31}$$

$$T_2 = \left|\frac{c_2}{a_2}\right|^2 = \left[\frac{\alpha_2 - \left|\cos(\frac{\Delta\varphi_2}{2})\right|}{1 - \alpha_2\left|\cos(\frac{\Delta\varphi_2}{2})\right|}\right]^2, \tag{4.32}$$

$$T_3 = \left|\frac{c_3}{a_3}\right|^2 = \left[\frac{\alpha_3 - \left|\cos(\frac{\Delta\varphi_3}{2})\right|}{1 - \alpha_3\left|\cos(\frac{\Delta\varphi_3}{2})\right|}\right]^2, \tag{4.33}$$

$$T_4 = \left|\frac{c_4}{a_4}\right|^2 = \left[\frac{\alpha_4 - \left|\cos(\frac{\Delta\varphi_4}{2})\right|}{1 - \alpha_4\left|\cos(\frac{\Delta\varphi_4}{2})\right|}\right]^2, \tag{4.34}$$

where α_1, α_2, α_3, and α_4 are round trip transmissions of light propagation through the four microring resonators [27] depending the losses of light propagation from output ports c_5, c_6, c_7, c_8 back to input ports a_5, a_6, a_7, a_8; for a lossless resonator $\alpha = 1$. The proposed structure can be viewed as a sensor with four channel sensing windows, which

are separated with four power transmission characteristics T_1, T_2, T_3, T_4 and four sensitivities S_1, S_2, S_3, S_4. This means that the proposed sensor is able to monitor four target chemicals simultaneously. Their sensitivities can be expressed by:

$$S_1 = \frac{\partial T_1}{\partial n_c},\ S_2 = \frac{\partial T_2}{\partial n_c},\ S_3 = \frac{\partial T_3}{\partial n_c},\ S_4 = \frac{\partial T_4}{\partial n_c}. \tag{4.35}$$

Fig. 4.19 compares the normalized transmission for the proposed sensor with $\alpha_1 = 0.99,\ 0.98,\ 0.97$ and 0.90 to that for the conventional MZI, as functions of the total relative phase $\Delta\varphi$. Given that the sensitivity is linearly proportional to the slope of the power transfer characteristics. Fig. 4.3 shows that the proposed sensor should have a higher sensitivity to a change in the refractive index of the analyte than the conventional MZI, when biased for operation with the region of large slope near $\Delta\varphi_1 = 0$.

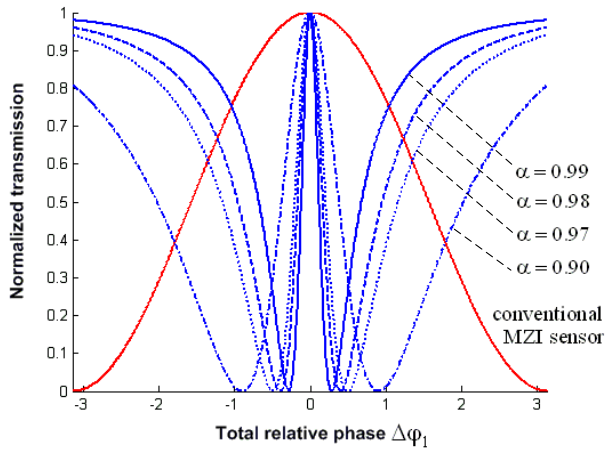

Fig. 4.19. Normalized optical transmissions as functions of total relative phase for the proposed sensor with $\alpha_1 = 0.99,\ 0.98,\ 0.97$ and 0.90 and conventional MZI sensor.

Fig. 4.20 shows the effective index change $\delta n_{eff,a}$ due to the ambient change for silicon nanowire waveguides having a width of 500 nm. From this simulation, one can see that the effective index $n_{eff,a}$ increases almost linearly in the change in the refractive index of ambient material, i.e., the waveguide sensitivity factor is almost a constant.

From the simulation results of Fig. 4.20, the sensitivities of the proposed sensor and the conventional MZI with the active region length of $L_a = 50\,\mu m$, $L_a = 100\,\mu m$ and $L_a = 500\,\mu m$ are plotted in Fig. 4.21. The simulations obviously show that the sensitivity of the proposed sensor is much higher than the sensitivity of the conventional MZI sensor.

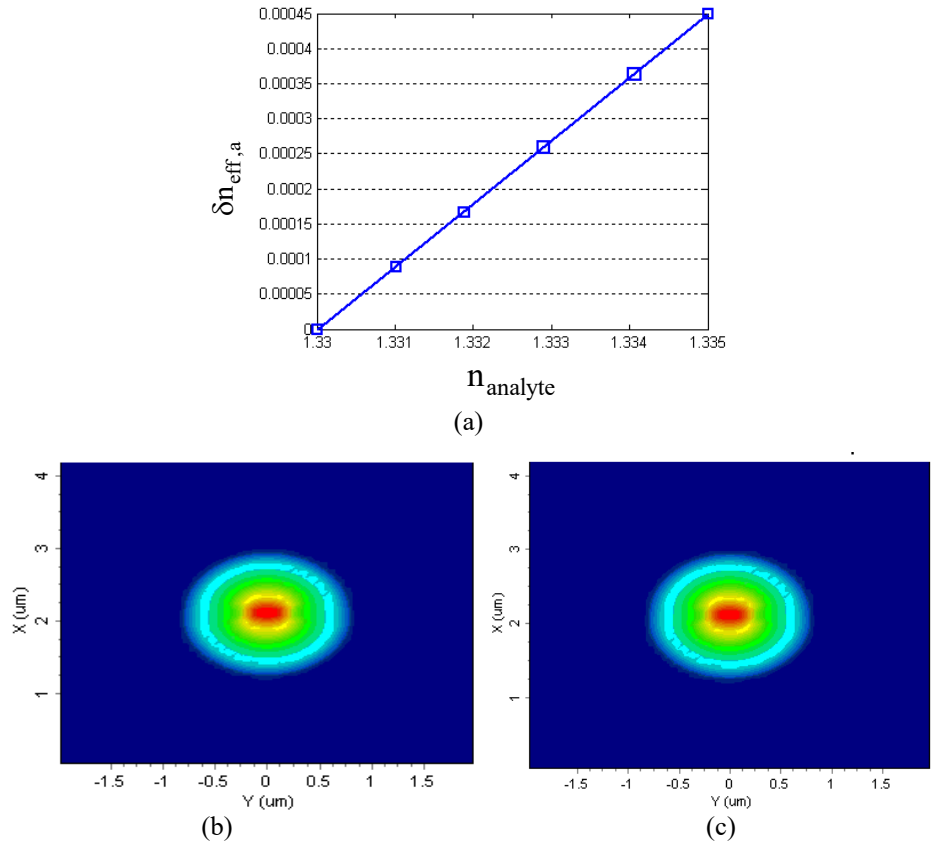

Fig. 4.20. (a) The change of the effective index as the increase of refractive index of the analyte for silicon nanowire waveguides, (b) optical field profile for $n_{analyte} = 1.33$ and (c) optical field profile for $n_{analyte} = 1.335$.

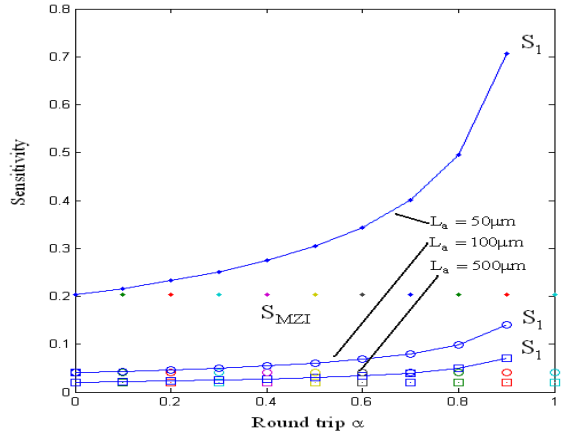

Fig. 4.21. Sensitivity of the proposed sensor for sensing window S1 and the conventional MZI sensor versus the round trip transmissivity of the first microring resonator.

4.7. Conclusions

We have presented novel sensor structures based on the integration of 4×4, 6×6 and 8×8 multimode interference structure and microring resonators. The proposed sensor structures can detect two, three and four chemical or biological elements simultaneously. Our sensor structure can be realized on silicon photonics that has advantages of compatibility with CMOS fabrication technology and compactness. It has been shown that our proposed sensors can provide a very high sensitivity compared with the conventional MZI sensor.

References

[1]. V. M. N. Passaro, F. Dell'Olio, B. Casamassima, et al., Guided-wave optical biosensors, *Sensors*, Vol. 7, 2007, pp. 508-536.
[2]. C. Ciminelli, C. M. Campanella, F. Dell'Olio, et al., Label-free optical resonant sensors for biochemical applications, *Progress in Quantum Electronics*, Vol. 37, 2013, pp. 51-107.
[3]. W. Wang (Ed.), Advances in Chemical Sensors, *InTech*, 2012.
[4]. L. Shi, Y. Xu, W. Tan, et al., Simulation of optical microfiber loop resonators for ambient refractive index sensing, *Sensors*, Vol. 7, 2007, pp. 689-696.
[5]. H. Yi, D. S. Citrin, Z. Zhou, Highly sensitive silicon microring sensor with sharp asymmetrical resonance, *Optics Express*, Vol. 18, 2010, pp. 2967-2972.
[6]. Z. Xia, Y. Chen, Z. Zhou, Dual waveguide coupled microring resonator sensor based on intensity detection, *IEEE Journal of Quantum Electronics*, Vol. 44, 2008, pp. 100-107.
[7]. V. M. Passaro, F. Dell'Olio, F. Leonardis, Ammonia optical sensing by microring resonators, *Sensors*, Vol. 7, 2007, pp. 2741-2749.
[8]. C. Lerma Arce, K. De Vos, T. Claes et al., Silicon-on-insulator microring resonator sensor integrated on an optical fiber facet, *IEEE Photonics Technology Letters*, Vol. 23, 2011, pp. 890-892.
[9]. T.-T. Le, Realization of a multichannel chemical and biological sensor using 6×6 Multimode interference structures, *International Journal of Information and Electronics Engineering*, Singapore, Vol. 2, 2011, pp. 240-244.
[10]. T.-T. Le, Microring resonator based on 3×3 general multimode interference structures using silicon waveguides for highly sensitive sensing and optical communication applications, *International Journal of Applied Science and Engineering*, Vol. 11, 2013, pp. 31-39.
[11]. K. De Vos, J. Girones, T. Claes, et al., Multiplexed antibody detection with an array of Silicon-on-Insulator microring resonators, *IEEE Photonics Journal*, Vol. 1, 2009, pp. 225-235.
[12]. D. Dai, Highly sensitive digital optical sensor based on cascaded high-Q ring-resonators, *Optics Express*, Vol. 17, 2009, pp. 23817-23822.
[13]. A. F. Gavela, D. G. García, C. Jhonattan Ramirez, et al., Last advances in silicon-based optical biosensors, *Sensors*, 2016, Vol. 16, 285
[14]. X. Han, Y. Shao, X. Han, et al., Athermal optical waveguide microring biosensor with intensity interrogation, *Optics Communications*, Vol. 356, 2015, pp. 41-48.
[15]. Y. Chen, Z. Li, H. Yi, et al., Microring resonator for glucose sensing applications, *Frontiers of Optoelectronics in China*, Vol. 2, 2009, pp. 304-307.
[16]. G.-D. Kim, G.-S. Son, H.-S. Lee, et al., Integrated photonic glucose biosensor using a vertically coupled microring resonator in polymers, *Optics Communications*, Vol. 281, 2008, pp. 4644-4647.

[17]. C. Errando-Herranz, F. Saharil, A. M. Romero, et al., Integration of microfluidics with grating coupled silicon photonic sensors by one-step combined photopatterning and molding of OSTE, *Optics Express*, Vol. 21, 2013, pp. 21293-21298.
[18]. T.-T. Le, Multimode Interference Structures for Photonic Signal Processing, *LAP Lambert Academic Publishing*, 2010.
[19]. J. M. Heaton, R. M. Jenkins, General matrix theory of self-imaging in multimode interference (MMI) couplers, *IEEE Photonics Technology Letters*, Vol. 11, 1999, pp. 212-214.
[20]. N. S Lagali, The general Mach-Zehnder interferometer using multimode interference coupler for optical communication network, PhD Thesis, *University of Alberta*, Canada, 2000.
[21]. T.-T. Le, L. Cahill, All optical signal processing circuits using multimode interference structures on silicon waveguides, in 4G Wireless Communication Networks: Design Planning and Applications (J. I. Agbinya, M. C. Aguayo-Torres, et al., Eds.), *River Publisher*, 2013.
[22]. A. Yariv, Universal relations for coupling of optical power between microresonators and dielectric waveguides, *Electronics Letters*, Vol. 36, 2000, pp. 321-322.
[23]. D.-T. Le, T.-T. Le, Coupled Resonator Induced Transparency (CRIT) based on interference effect in 4×4 MMI coupler, *International Journal of Computer Systems (IJCS)*, Vol. 4, 2017, pp. 95-98.
[24]. T.-T. Le, All-optical Karhunen-Loeve transform using multimode interference structures on silicon nanowires, *Journal of Optical Communications*, Vol. 32, 2011, pp. 217-220.
[25]. L. B. Soldano, E. C. M. Pennings, Optical multi-mode interference devices based on self-imaging:principles and applications, *IEEE Journal of Lightwave Technology*, Vol. 13, 1995, pp. 615-627.
[26]. T.-T. Le, L. Cahill, Generation of two Fano resonances using 4×4 multimode interference structures on silicon waveguides*, Optics Communications*, Vol. 301-302, 2013, pp. 100-105.
[27]. W. Green, R. Lee, G. DeRose, et al., Hybrid InGaAsP-InP Mach-Zehnder racetrack resonator for thermooptic switching and coupling control, *Optics Express*, Vol. 13, 2005, pp. 1651-1659.
[28]. T.-T. Le, L. Cahill, The design of 4×4 multimode interference coupler based microring resonators on an SOI platform, *Journal of Telecommunications and Information Technology*, Poland, 2009, pp. 98-102.
[29]. D.-T. Le, M.-C. Nguyen, T.-T. Le, Fast and slow light enhancement using cascaded microring resonators with the Sagnac reflector, *Optik - International Journal for Light and Electron Optics*, Vol. 131, 2017, pp. 292–301.
[30]. X. Liang, Q. Zhang, H. Jiang, Quantitative reconstruction of refractive index distribution and imaging of glucose concentration by using diffusing light, *Applied Optics*, Vol. 45, 2006, pp. 8360-8365.
[31]. C. Ciminelli, F. Dell'Olio, D. Conteduca, et al., High performance SOI microring resonator for biochemical sensing, *Optics & Laser Technology*, Vol. 59, 2014, pp. 60-67.
[32]. T.-T. Le, Two-channel highly sensitive sensors based on 4×4 multimode interference couplers, *Photonic Sensors*, 2017, pp. 1-8.
[33]. O. A. Marsh, Y. Xiong, W. N. Ye, Slot waveguide ring-assisted Mach–Zehnder interferometer for sensing applications, *IEEE Journal of Selected Topics in Quantum Electronics*, Vol. 23, 2017, pp. 440-443.
[34]. J. Hu, X. Sun, A. Agarwal, et al., Design guidelines for optical resonator biochemical sensors, *Journal of the Optical Society of America B*, Vol. 26, 2009, pp. 1032-1041.
[35]. Y. Chen, Y. L. Ding, and Z. Y. Li, Ethanol sensor based on microring resonator, *Advanced Materials Research*, Vol. 655-657, 2013, pp. 669-672.
[36]. S. Manipatruni, R. K. Dokania, B. Schmidt, et al., Wide temperature range operation of micrometer-scale silicon electro-optic modulators, *Optics Letters*, Vol. 33, 2008, pp. 2185-2187.

[37]. M. Han, A. Wang, Temperature compensation of optical microresonators using a surface layer with negative thermo-optic coefficient, *Optics Letters*, Vol. 32, 2007, pp. 1800-1802.
[38]. K. B. Gylfason, A. M. Romero, H. Sohlström, Reducing the temperature sensitivity of SOI waveguide-based biosensors, *Proceedings of SPIE*, Vol. 8431, 2012, pp. 84310F (1-15).
[39]. C.-T. Wang, C.-Y. Wang, J.-H. Yu, et al., Highly sensitive optical temperature sensor based on a SiN micro-ring resonator with liquid crystal cladding, *Optics Express*, Vol. 24, 2016, pp. 1002-1007.
[40]. F. Qiu, F. Yu, A. M. Spring, et al., Athermal silicon nitride ring resonator by photobleaching of Disperse Red 1-doped poly (methyl methacrylate) polymer, *Optics Letters*, Vol. 37, 2012, pp. 4086-4088.
[41]. B. Guha, B. B. C. Kyotoku, M. Lipson, CMOS-compatible athermal silicon microring resonators, *Optics Express*, Vol. 18, 2010, pp. 3487-3493.
[42]. S. T. Fard, V. Donzella, S. A. Schmidt, et al., Performance of ultra-thin SOI-based resonators for sensing applications, *Optics Express*, Vol. 22, 2014, pp. 14166-14179.
[43]. T.-T. Le, The design of microresonators based on multimode interference couplers on an SOI platform, in *Proceedings of the 3rd International Conference on Communications and Electronics (ICCE'10)*, Nha Trang, Vietnam, 11-13 August, 2010.